photochem

Review

Solid State Nanostructured Metal Oxides as Photocatalysts and Their Application in Pollutant Degradation: A Review

Carlos Díaz [1,*], Marjorie Segovia [2] and Maria Luisa Valenzuela [3,*]

[1] Departamento de Química, Facultad de Ciencias, Universidad de Chile, Las Palmeras 3425, Santiago 7750000, Chile
[2] Facultad de Ingeniería, Pontificia Universidad Católica de Chile, Vicuña Mackenna 4860, Santiago 8331150, Chile
[3] Grupo de InvestigaciÓn en Energía y Procesos Sustentables, Instituto de Ciencias Químicas Aplicadas, Facultad de Ingeniería, Universidad Autónoma de Chile, Av. El Llano Subercaseaux 2801, Santiago 8910060, Chile
* Correspondence: cdiaz@uchile.cl (C.D.); maria.valenzuela@uautonoma.cl (M.L.V.)

Abstract: Most dyes used in various industries are toxic and carcinogenic, thus posing a serious hazard to humans as well as to the marine ecosystem. Therefore, the impact of dyes released into the environment has been studied extensively in the last few years. Heterogeneous photocatalysis has proved to be an efficient tool for degrading both atmospheric and aquatic organic contaminants. It uses the sunlight in the presence of a semiconductor photocatalyst to accelerate the remediation of environmental contaminants and the destruction of highly toxic molecules. To date, photocatalysis has been considered one of the most appealing options for wastewater treatment due to its great potential and high efficiency by using sunlight to remove organic pollutants and harmful bacteria with the aid of a solid photocatalyst. Among the photocatalysts currently used, nanostructured metal oxide semiconductors have been among the most effective. This review paper presents an overview of the recent research improvements on the degradation of dyes by using nanostructured metal oxide semiconductors obtained by a solid-state method. Metal oxides obtained by this method exhibited better photocatalytic efficiency than nanostructured metal oxides obtained using other solution methods in several cases. The present review discusses examples of various nanostructured transition metal oxides—such as TiO_2, Fe_2O_3, NiO, ReO_3, IrO_2, Rh_2O_3, Rh/RhO_2, and the actinide ThO_2—used as photocatalysts on methylene blue. It was found that photocatalytic efficiency depends not only on the bandgap of the metal oxide but also on its morphology. Porous nanostructured metal oxides tend to present higher photocatalytic efficiency than metal oxides with a similar band gap.

Keywords: photocatalyst; metal oxides; environmental remediation; solid state

check for updates

Citation: Díaz, C.; Segovia, M.; Valenzuela, M.L. Solid State Nanostructured Metal Oxides as Photocatalysts and Their Application in Pollutant Degradation: A Review. *Photochem* **2022**, *2*, 609–627. https://doi.org/10.3390/photochem2030041

Academic Editor: Vincenzo Vaiano

Received: 2 June 2022
Accepted: 23 July 2022
Published: 5 August 2022

1. Introduction

Currently, researchers and scientists are becoming increasingly interested in metal oxide nanostructures due to their important technological applications in electronic and optoelectronic devices, sensors, medicines, and renewable energy sources. Reducing the size of materials (metal oxides) to nano-level imparts properties different from the bulk or crystalline forms; these nanoparticles demonstrate behaviors characteristic of isolated atoms and molecules [1–5].

Industrial plants generate increasing amounts of wastewater, which often causes severe environmental problems [6,7]. Wastewater produced in many industrial processes typically contains organic compounds that are toxic and not amenable to biological treatments [7]. There are several different types of organic pollutants, including dyes, phenols, biphenyls, pesticides, fertilizers, hydrocarbons, plasticizers, detergents, oils, greases, pharmaceuticals, proteins, carbohydrates, and so on [8].

Among the various physical, chemical, and biological technologies used in pollution control, advanced oxidation processes such as photocatalysis are being increasingly adopted in the destruction of organic contaminants due to their high efficiency, simplicity, good reproducibility, and ease of handling [8]. Heterogeneous photocatalysis possesses some critical advantages that have feasible applications in wastewater treatments, including: ambient operating temperatures and pressures, and the complete mineralization of contaminants and their intermediate compounds without leaving secondary pollutants. However, for large scale municipal applications, current photocatalytic water treatment systems are less attractive because they are more time consuming and have higher costs than other existing advanced oxidation techniques such as UV/H_2O_2, O_3/H_2O_2, and UV/O_3 technologies [9].

Therefore, semiconducting metal oxides have high potential due to their capability to generate charge carriers when stimulated with the required amount of energy, and to their applications in environmental remediation and electronics. Some semiconducting metal oxide synthesis methods are the chemical vapor deposition technique, the hydrothermal method, the laser ablation technique, and the electro-deposition method [10,11]. Out of these techniques, the hydrothermal method is the most user-friendly because of its reduced cost and ease of handling as well as being chemically reactive at low temperatures. However, other methods including the thermal decomposition of solids such as molecular complexes and macromolecular complexes [12] are gaining relevance due to their ease of preparation and final product purity.

An example of environmental remediation processes is the degradation of organic dyes [13] and the generation of clean energies such as "green hydrogen" [14].

In this context, one of the main applications of nanostructured metal oxides is the photocatalytic degradation of organic pollutants, which is in the field of environmental remediation.

The main characteristics that a suitable metal oxide photocatalytic system must have are [15]:

1. An adequate bandgap;
2. Suitable morphology;
3. High surface area;
4. Stability and reusability.

Semiconductor metal oxides with a bandgap near 3.2 eV are UV-light active, while semiconductor metal oxides with a bandgap near 2.7 eV are Visible-light active [16,17]. Metal oxides exhibiting these features—such as oxides of vanadium, chromium, titanium, zinc, tin, and cerium—follow similar primary photocatalytic processes such as light absorption, which induces a charge separation process with the formation of positive holes that can oxidize organic substrates. In this process, a metal oxide is activated with either UV light, visible light, or a combination of both, and photoexcited electrons are promoted from the valence band to the conduction band, forming an electron/hole pair (e^-/h^+). The photogenerated pair (e^-/h^+) can reduce and/or oxidize a compound adsorbed on the photocatalyst surface. A schematic representation of this process is shown in Figure 1.

As Figure 1 shows, the bandgap of the metal oxides dictates their photocatalytic activity; crucially, it establishes whether their energy matches or exceeds the band gap energy of the semiconductor. In Table 1, a summary of the bandgap values for the most common metal oxides along the periodic table is displayed. It is important to note that the bandgap values vary with the size of the nanoparticle, preparation method, doping, etc.

The photocatalytic activity of metal oxides comes from two sources [13]:

(i) Generation of $^\bullet$OH radicals by oxidation of OH^- anions;
(ii) Generation of $O_2{}^-$ radicals by reduction of O_2.
   Nanostructured metal oxide semiconductors have been widely used in photocatalytic redox processes because of their filled valence band (VB) and empty conduction band (CB) electronic configurations. When exposed to a photon with energy exceeding the bandgap ($h\nu > E_g$), it generates an electron-hole pair with one electron in VB pumped

into CB, leaving a hole behind in VB. The holes generated in VB have great oxidation capability, while the electrons in the CB have high reduction potential.

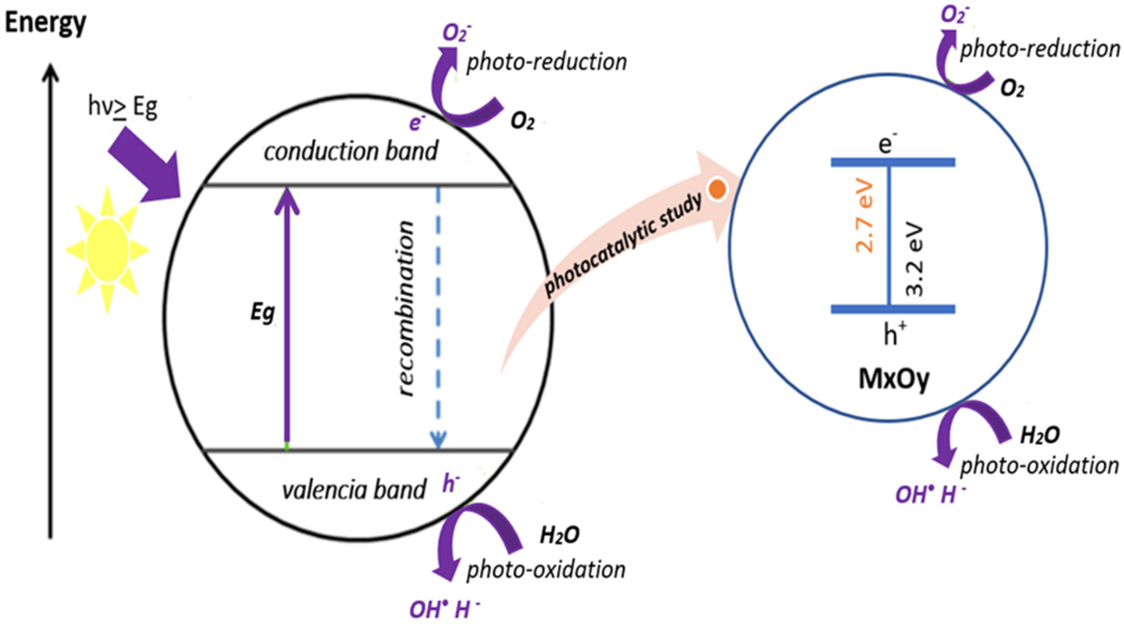

Figure 1. Photocatalytic activity of nanostructured metal oxides.

Table 1. Bandgap values for the main metal oxides along the periodic table.

Metal Oxides	Compounds	Bandgap (eV) [a,b]	Ref.
Metal transition	Cr_2O_3	3.2	[18]
	V_2O_5	2.3	[18]
	Co_3O_4	1.5	[18]
	TiO_2	3.3 (anatase)	[18]
	TiO_2	3.0 (rutile)	[18]
	Mn_2O_3	3.27	[19]
	WO_3	2.8	[19]
	MoO_3	3.14	[18]
	NiO	3.5	[19]
	Fe_2O_3	2.1	[18]
	Fe_3O_4	2.61	[19]
	Cu_2O	2.2	[18]
	CuO	1.6	[18]
Metal representative	ZnO	3.2,34	[19,20]
	SnO_2	4.2	[19]
	Ga_2O_3	4.85	[19]
	Sb_2O_3	4.49	[19]
Lanthanides	CeO_2	3.0–3.6	[19]
	La_2O_3	4.3	[19]
Actinides	ThO_2	3.1	[21]

[a] Values from references: [17–22]. [b] Other similar values are reported for some of the metal oxides.

These highly-reactive electrons and holes participate in the photocatalytic organic degradation.

As mentioned above, the factors relevant for a photocatalyst to be efficient include adequate bandgap, suitable morphology, high surface area, stability, and reusability.

Whether a given nanostructured metal oxide meets these characteristics depends on its preparation method. For instance, TiO_2 is one of the most used and efficient metal oxides for the photocatalytic degradation of several organic dye pollutants [23]. However, its relative efficiency depends on the preparation method, which in turn determines its bandgap, morphology, surface area, stability and reusability.

For instance, the dependence of the catalytic effectiveness of TiO_2 on the preparation method is illustrated in Table 2.

Table 2. Photocatalytic Performances and Key Factors (Crystal Phase, Size and Morphology) of Different TiO_2 Materials in the Degradation of Organic Water Pollutants [24].

Organic Water Pollutant	Photocatalyst (Concentration)	Irradiation Light	Reaction Kinetic	Removal %	Irradiation Time
MB (1×10^{-5} M)	TiO_2 anatase. 1 g $\times$ Lt^{-1} with 340 nm cut-off filter, 330 nm $> \lambda >$ 680 nm	Xe lamp (150 W)	Pseudo first-order kinetic	86.5%	25 min
MB (10 ppm)	TiO_2 nanoparticles (2.5 g L^{-1})	UV lamp (40 W)	Langmuir–Hinshelwood Pseudo first-order kinetic	71%	60 min
MB (50 ppm)	TiO_2 nanofibers	Xenon lamp UV-vis (150 W) with AM 1.5 G filter $\lambda >$ 400 nm	NM	100%	180 min
MB(10 mgL^{-1})	TiO_2 nanotubes (0.16 g L^{-1})	xenon visible light (500 W)	NM	99.1%	40 min
MB (0.01 mM)	mesoporous TiO_2 0.17 g L^{-1})	UV light irradiation using eight tubes with a power source of 6 W, λ = 365 nm	NM	85%	60 min
MB (0.75 $\times$ 10^{-5} M)	Hollow titania micro-spheres (HTS)	UV lamp 15 W	Pseudo first-order kinetic	53%	90 min
MB (1 mM)	TiO_2 nanoparticles	Blacklight lamp (1 mW)	NM	45%	20 min
Other similar organic water pollutants malachite green, MG (10 ppm)	TiO_2nanoparticles (2.5 g L^{-1})	UV lamp (40 W)	Langmuir–Hinshelwood Pseudo first-order kinetic	78%	60 min
Rhodamine B, RhB, and methyl orange MO (0.01 mM)	TiO_2 hollow tetragonal nanocone (0.1 g L^{-1})	full-arc Xe lamp (300 W) with a cutoff filter, $\lambda >$ 420 nm	NM	95.0% for RhB, 90.7% for MO	30 min
Bisphenol A BPA, (200 µM)	TiO_2 powder, Degussa P25 (0.5 g L^{-1})	Xe arc lamp (300 W), IR water filter and cutoff filter, $\lambda >$ 420 nm	Pseudo first-order kinetic	75% for BPA	4 h
acetaminophen, Ace (1.3 µM)	TiO_2 powder, Degussa P25 (NM)	UVA/LED λ_{max} = 366 nm	NM	100%	8 min
RhB (NM)	TiO_2 nanopowder (0.3 g L^{-1})	visible light $\lambda >$ 420 nm	NM	90%	5 h
Methyl orange 4 $\times$ 10^{-5} M	TiO_2 powder (10 mg)	Xe lamp 300 W	NM	90%	3 h

The E_g bandgap also exhibits an inverse dependence on particle size. For instance, theoretical studies have explained this relationship with the following expression [25]:

$$E_g^* \cong E_g^{bulk} + \frac{\hbar^2 \pi^2}{2er^2}\left(\frac{1}{m_e} + \frac{1}{m_h}\right) - \frac{1.8e^2}{4\pi\varepsilon\varepsilon_0 r} \tag{1}$$

where E_g bulk is the bulk energy gap, r is the particle radius, m_e is the effective mass of the electrons, m_h is the effective mass of the holes, ε is the relative permittivity, ε_0 is the permittivity of free space, $\hbar$ is Plancks constant divided by 2π, and e is the charge of the electron.

The experimental inverse, E_g vs. particle size, has been observed for several nanostructured metal oxide nanoparticles [25–27], including ZnO, Fe_2O_3, Co_3O_4, NiO and SnO_2.

On the other hand, the bandgap can also be modified by doping. In general, doping decreases the bandgap, as is reported in the case of ZnO/Mn^{2+}, ZnO/Cu and TiO_2/doping, among others [24]. Some of the most studied are the TiO_2/dopant and ZnO/dopant. Tables 3 and 4 summarize some of the results of M_xO_y/dopant systems. One of the explanations for this decrease in bandgap after doping is the increase in surface area. The increased surface area of the photocatalyst also increases the photodegradation of dye pollutants. This is because materials with a large surface area have more active sites than materials with a low surface area. This is illustrated in Table 3.

Table 3. Photocatalytic improvement parameter of various ZnO nano-photocatalysts (Adapted from reference [24]).

Photocatalyst	Bandgap	Surface Area
Bi^{3+}-ZnO	3.15–2.6	Increase
Co-ZnO	3.34–3.06	Increase
N-ZnO	3.15–2.86	Increase
F-ZnO	3.35–2.51	Increase
Fe-ZnO	3.24–3.16	Increase
Ag/ZnO	3.30–3.21	Increase
B/ZnO	3.2–3.1	Increase
Bi-TiO_2	2.99–3.08	Decrease
Ni-TiO_2	3.02, 2.99–3.03	
Ag-TiO_2	3.0–2.6	Increase
Fe-TiO_2	3.2–2.98	Increase
N-TiO_2	3.1–2.7	Increase
Ti/WO_3	3.4–3.31	Decrease
Zn-WO_3	3.2–3.12	Slight decrease
Fe-SnO_2	3.8–1.65	Increase
Zn-SnO_2	3.50–3.17	Increase
Cu-SnO_2	3.02–2.2	Increase

As mentioned before, ZnO is one of the most common and effective photocatalysts for the photodegradation of organic dye pollutants. ZnO is insoluble in water, existing in the form of a white powder, and it is extracted from the mineral Zincite through synthetic methods. Plastic, rubber, glass, ceramic, and cement industries use ZnO in various processes. ZnO is an n-type semiconductor with high bandgap energy that belongs to group II–IV of the periodic table [26,27]. ZnO is chemically stable, nontoxic, and inexpensive. It possesses high radiation hardness, effective transparency, remarkable optical absorption in the UV range, and outstanding thermal properties. Due to these characteristics, ZnO is used in a number of applications, such as optoelectronics, solar cells, medicine, catalysis, photocatalysis, and as an antibacterial agent. Doping in ZnO produces a decrease in the bandgap, which enhances photocatalytic efficiency. In Table 4, some doped ZnO are shown.

Table 4. Photocatalytic improvement performance of various ZnO nano-photocatalysts (Adapted from reference [24]).

N°	Composite	Synthesis Method	Pollutant for Degradation	PC Performance	Irradiation
1	Co-ZnO	Sol-gel	MB	3 at.% Co-ZnO exhibited 92% degradation in 60 min.	Visible light
2	La-doped ZnO	Hydrothermal oxidation	MO and MB	Best PCA observed by S0.005 due to defects.	UV light
3	Pd/ZnO	Microwave hydrothermal, borohydride and photoreduction	CR	Pd/ZnO synthesized by borohydride method has the highest PCA compared to other routes.	UV light
4	C, N co-doped ZnO	Two-step pyrolysis	MB	6C25 showed the best degradation due to its larger number of active sites.	Solar stimulated light
5	X-ZnO (X = Li, Al, N, P)	Mass production technology	RhB	PCA decreased as follows: N > Li > P > Al	Sunlight
6	Fe-doped ZnO	Combustion	BPA	FexZn$_{1-x}$O (where x = 0.03) showed noticeable efficacy in the series.	Sunlight
7	Gd-ZnO films	RF magnetron sputtering	MB	0.7 at.% Gd-ZnO exhibited higher PCA than ZnO.	UV light
8	Au-ZnO Ag-ZnO	Combustion	MB	Ag-ZnO demonstrated better activity than Au-ZnO.	UV light
9	Eu^{3+}-doped ZnO	Coprecipitation	RhB	Doped ZnO (100%) degraded dye faster than ZnO.	UV light
10	Ce-ZnO	Hydrothermal	Pharmaceutica	Nizatidine, levofloxacin and acetaminophen degraded around 95% within 4 h.	UV light
11	Cu-ZnO	Chemical growth	MO and MB	Increase in PC efficiency was 57.5% for MO and 60% for MB in 180 min.	UV light
12	B-ZnO	Sol-gel	CN$^-$	Doped sample with 1.5 wt% exhibited 89% degradation whereas pure ZnO exhibited 75%.	Solar stimulated light
13	In-ZnO	Plasma assisted chemical vapors	MB	4 at.% In-ZnO showed improved PCA compared to ZnO and 8 at.% In-ZnO.	Solar stimulated light
14	Sm-ZnO	Chemical precipitation	MB	Zn$_{1-x}$Sm$_x$O x = 0.04 expressed maximum PC degradation (94.94%).	Visible light
15	WO$_3$-doped ZnO	hydrothermal	Diazinon	10 mg/L diazinon, 10 g/cm^{-2} 2% O$_3$-ZnO exhibited 99% degradation in 180 min.	UV light

Titanium dioxide, TiO$_2$, is also known as Titania or titanium (IV) oxide. TiO$_2$ is the most promising photocatalyst since it possesses long-term chemical and physical stability along with low production costs [28]. It has a wide bandgap (3.0–3.2 eV) in the UV light range and exhibits three polymorphs, namely rutile, anatase, and brookite. Among these three phases, rutile is the most stable phase; the others are metastable, but they can transform into rutile phase irreversibly at elevated temperatures. Furthermore, the TiO$_2$ photocatalyst has important uses in water treatment, lithium-ion batteries, sensors, catalysis, antibacterial, and anticancer applications [29–31]. Table 5 shows some examples of TiO$_2$/dopants and their photocatalytic activity toward different organic dye pollutants.

Table 5. Summary of various TiO_2 nano-photocatalysts, pollutants, and irradiation sources along with their measured Photocatalysis (Adapted from reference [24]).

N°	Doped	Pollutants	PCA	Irradiation Source
1	Ce-TiO_2 La-TiO_2 V-TiO_2	RhB	1.0%-Ce-TiO_2 > 1.0%-V-TiO_2 > undoped TiO_2 > 1.0%-La-TiO_2 showed degradation (%) 83.43 > 53.74 > 21.56 > 11.09, respectively.	Solar light
2	PF co-doped anatase TiO_2	MO	It demonstrated excellent PCA compared to undoped TiO_2, F-TiO_2, P-TiO_2 and Degussa P25.	Full-spectrum light
3	Ga-doped TiO_2nanopowder	MO	0.6 mol% Ga-TiO_2 demonstrated up to 82% degradation.	Visible light
4	F, N co-doped TiO_2	MB	97.31% degradation was achieved within 5 h.	Visible light
5	Nd-TiO_2 film	MB	0.1% Nd-doped TiO_2 showed maximum degradation (92%).	UV light
6	Moroccan natural P-TiO_2	IC	Its degradation increased at high values of pH, initial concentration and amount of catalyst.	UV light
7	Nb_2O_5-TiO_2	MB	5 mol% expressed the highest PCA under visible light and equal efficiency as TiO_2 under UV.	UV and Visible light
8	Mesoporous Ag-TiO_2	MO	TiO_2 with the lowest content of Ag exhibited higher PCA.	UV and solar light
9	Fe^{3+}-TiO_2	CV	Degradation kinetics rate increased with an increase in iron content.	UV
10	Ru/TiO_2	2-CP	0.4 wt% Ru/TiO_2 showed high PCA using UV light and 0.2% Ru/TiO_2 using visible light.	UV and visible light
11	Gd-TiO_2	RhB	0.3% Gd-TiO_2 demonstrated the best PCA.	Visible light
12	C-TiO_2	RhB	More decolorization compared to fluorescence spectroscopy.	Visible light
13	Pd-TiO_2	MB and MO	Maximum degradation shown by 0.75 wt% Pd-TiO_2 for mixture of dyes and 0.5 wt% Pd-TiO_2 for single dye.	Visible or solar light
14	Graphene/TiO_2	BPA	It showed remarkable PCA compared to pure TiO_2.	Solar light
15	Ni/TiO_2	Malathion	94% degradation achieved.	UV light

2. Materials and Methods

Nanostructured Metal Oxides Preparation Methods

Several solution methods have been developed for synthesizing metal or metal oxide nanoparticles, such as the solvothermal, hydrothermal, and sol-gel methods [10,11]. Several of these nanostructured metal oxides have been suitable for photocatalytic degradation of organic dye pollutants. Usually, the preparation of nanostructured metal oxides for photocatalysis involves some solution method. However, for some of these methods, drawbacks like the aggregation of the NPs during the adsorption stage cause a reduction in the efficiency of the desired application [32–34]. When the metal or metal oxide is obtained as a colloid, as is commonly observed, their separation by centrifugation often produces agglomeration of the NPS [34]. To solve this type of problem, a solid-state method is used in which the metal nanoparticles are generally obtained as solid pure phase material. Therefore, the solventless synthesis of nanostructures is highly significant due to its economical, eco-friendly, and industrially viable nature. However, the development of new solid-state methods to prepare metallic nanostructured materials is a constant challenge. We have previously described a new solid-state method to synthesize metallic nanostructured nanomaterials from the pyrolysis of metallic and organometallic derivatives of poly- and oligo-phosphazene under air and at 800 °C [35–38]. Metallic nanostructured materials of the type M, M_xO_y, and $M_xP_yO_z$ are obtained depending on the nature of the metal. Another method—used when the respective metallic or organometallic derivative is not possible to prepare—uses MLn/$[NP(O_2C_{12}H_8)]_3$ mixtures [39–41]. However, in several of these systems, the M or M_xO_y phase is accompanied by a phosphate phase. These methods have been discussed in detail in several papers [35–41] and books [32,33,42–44]. When we used a polymer that does not contain phosphorus in its polymeric chain—such as the chitosan MXn and PS-co-4-PVP MXn macromolecular precursors (MXn = metallic salt)—and then subjected it to solid-state pyrolysis under air and at 800 °C (see Figure 2), pure phase nanostructured M_xO_y were obtained [45–57]. Now we will discuss the use of these nanostructured metal oxides M_xO_y obtained by this method in the degradation of organic dye pollutants.

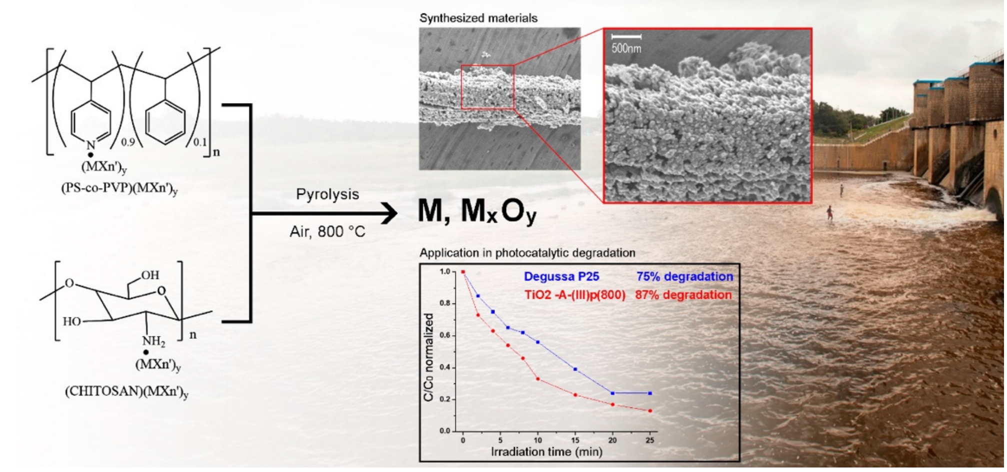

Figure 2. Schematic representation of the solid-state method and its application in environmental remediation.

3. Results

3.1. TiO_2

The titania to be used as photocatalyst was obtained by pyrolysis of the (Cp_2TiCl_2)(Quitosano) (I),(Cp_2TiCl_2)(PS-co-4-PVP) (II), $(TiOSO_4)$(Chitosan) (III), $(TiOSO_4)$(PS-co-4-PVP) (IV), $(TiO(acac)_2)$(Chitosan) (V), and $(TiO(acac)_2)$(PS-co-4-PVP) (VI) macromolecular precursors under air and at several temperatures (500 °C, 600 °C, 700 °C, and 800 °C [23]. The bandgaps of the TiO_2 obtained using these precursors are displayed in Table 6. The values range from 3.21 to 3.72 eV, which are adequate for photocatalytic degradation of organic dyes using UV-visible irradiation.

The results of the photocatalytic degradation of methylene blue are shown in Table 7.

As can be seen in Table 7, the most efficient catalytic degradation arises from the TiO_2 produced from the TiO_2-A-(III)p(800) system precursors, with 87% degradation after 25 min. Based on this table, the photocatalytic efficiency could be expressed by the following multifactorial relationship:

$$PE = a \text{ bandgap} + b \text{ particle morphology} + c \text{ particle size} + d \text{ Titania phase} + e \text{ pyrolysis temperature} \quad (2)$$

where PE is photocatalytic efficacy and the Titania phase can be anatase, rutile, or brookita. In the case of TiO_2 obtained by our solid-state method using TiO_2-A-(III)p(800) as the precursor, factor b is highly porous (see Figure 3) since, as it is known, the anatase form is the most efficient phase as a photocatalyst and, in solid-state, the temperature of the thermal treatment is crucial to determine morphology and particle size. In this case, factor a does not appear to be very important since, as shown in Table 7, the values are similar.

Table 6. Bandgap for TiO_2 obtained using different precursors and temperatures (Adapted from reference [23]).

TiO_2-(I)p			**TiO_2-(II)p**		
Temperature (°C)	Phase	Bandgap (eV)	Temperature (°C)	Phase	Bandgap (eV)
500	Anatase	3.66	500	Anatase	3.43
600	Mixture	3.43	600	Anatase	3.30
700	Mixture	3.63	700	Anatase	3.22
800	Rutile	3.40	800	Mixture	3.27
TiO_2-(III)p			**TiO_2-(IV)p**		
Temperature (°C)	Phase	Bandgap (eV)	Temperature (°C)	Phase	Bandgap (eV)
500	Anatase	3.32	500	Anatase	3.53
600	Anatase	3.43	600	Anatase	3.45
700	Anatase	3.28	700	Mixture	3.37
800	Anatase	3.65	800	Mixture	3.38
TiO_2-(V)p			**TiO_2-(VI)p**		
Temperature (°C)	Phase	Bandgap (eV)	Temperature (°C)	Phase	Bandgap (eV)
500	Anatase	3.47	500	Anatase	3.72
600	Anatase	3.42	600	Mixture	3.57
700	Mixture	3.21	700	Mixture	3.36
800	Mixture	3.33	800	Rutile	3.24

Table 7. Kinetic data for degradation of methylene blue with nanostructured TiO_2 (Adapted from reference [23]).

Sample	**Apparent Photodegradation Rate Constant k (10^{-2} min^{-1})**	**Degradation η (%)**	**R^2 (%)**
TiO_2-Anatase-(I)p 500 °C	0.40 ± 0.04	11	93.9
TiO_2-Mixture-(I)p 600 °C	0.80 ± 0.04	20	98.4
TiO_2-Mixture-(I)p 700 °C	0.06 ± 0.03	14	98.0
TiO_2-Rutile-(I)p 800 °C	1.30 ± 0.10	30	93.8
TiO_2-Anatase-(II)p 500 °C	0.40 ± 0.04	11	91.9
TiO_2-Anatase-(II)p 600 °C	0.33 ± 0.03	7	88.8
TiO_2-Anatase-(II)p 700 °C	0.40 ± 0.02	10	97.6
TiO_2-Mixture-(II)p 800 °C	1.00 ± 0.06	23	97.2
TiO_2-Anatase-(III)p 500 °C	3.90 ± 0.20	65	96.9
TiO_2-Anatase-(III)p 600 °C	4.10 ± 0.20	65	97.4
TiO_2-Anatase-(III)p 700 °C	2.00 ± 0.06	39	99.2
TiO_2-Anatase-(III)p 800 °C	7.13 ± 0.01	87	99.8
TiO_2-Anatase-(IV)p 500 °C	2.40 ± 0.01	45	97.8
TiO_2-Anatase-(IV)p 600 °C	3.10 ± 0.01	55	98.0
TiO_2-Mixture-(IV)p 700 °C	0.20 ± 0.02	5	91.1
TiO_2-Mixture-(IV)p 800 °C	4.00 ± 0.20	63	97.1
TiO_2-Anatase-(V)p 500 °C	3.40 ± 0.10	59	99.1
TiO_2-Anatase-(V)p 600 °C	1.30 ± 0.04	27	99.2
TiO_2-Mixture-(V)p 700 °C	1.30 ± 0.09	27	96.4
TiO_2-Mixture-(V)p 800 °C	0.60 ± 0.03	14	98.0
TiO_2-Anatase-(VI)p 500 °C	1.70 ± 0.03	34	99.7
TiO_2-Mixture-(VI)p 600 °C	2.40 ± 0.02	48	95.9
TiO_2-Mixture-(VI)p 700 °C	2.60 ± 0.02	51	94.6
TiO_2-Rutile-(VI)p 800 °C	0.50 ± 0.02	14	98.5

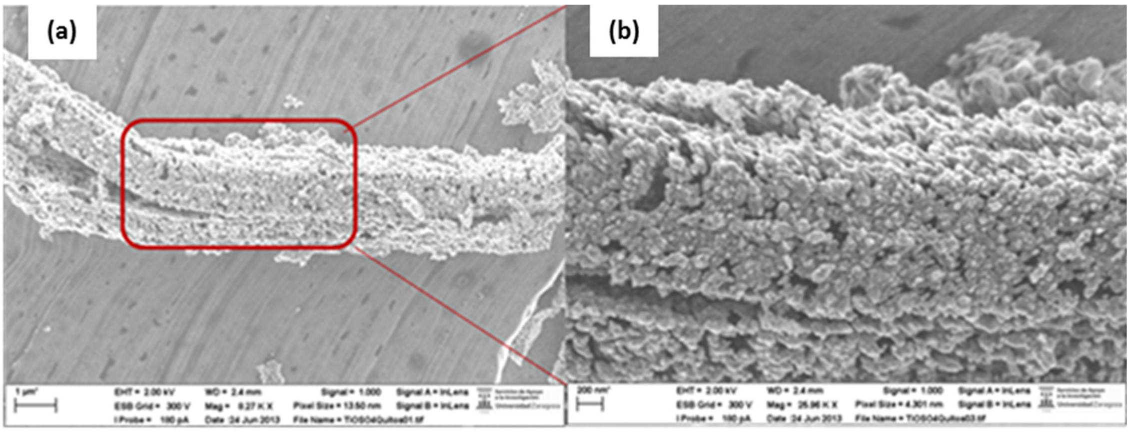

Figure 3. FE-SEM images of TiO_2-Anatase-(III)p(800) (**a**) and an amplification of a portion of the structure (**b**) (Adapted from reference [23]).

The results shown in Table 7 were obtained at pH 6.5; however, a pH effect study showed that, at alkaline pH 9.5, the degradation was 98% [23].

3.2. Fe_2O_3

Fe_2O_3 was prepared by pyrolysis of the Chitosan$(FeCl_2)_y$, Chitosan$(FeCl_3)_y$, PS-b-4-PVP$(FeCl_2)_y$, and PS-b-4-PVP$(FeCl_3)_y$ macromolecular complexes under air and at 800 °C [47]. The product was Fe_2O_3 in the hematite phase in all the cases. The bandgap of the as-prepared Fe_2O_3 ranged from 1.83 eV to 2.12 eV, which indicated an effective photocatalyst behavior under UV-visible irradiation (see Table 8).

Table 8. Kinetic data for the degradation of MB with α-Fe_2O_3 obtained from PS-co-4-PVP and chitosan macromolecular precursors (Adapted from reference [47]).

Precursor	E_g (eV)
Chitosan$(FeCl_3)$ 1:1	1.83
Chitosan$(FeCl_3)$ 1:5	2.15
PS-co-4-PVP$(FeCl_3)$ 1:1	2.12
Fe^{+3}-PS-co-4-PVP$(FeCl_3)$ 1:5	2.12
Chitosan$(FeCl_2)$ 1:1	2.15
Chitosan$(FeCl_2)$ 1:5	2.15
PS-co-4-PVP$(FeCl_2)$ 1:1	1.90
PS-co-4-PVP$(FeCl_2)$ 1:5	2.09

Some parameters for the degradation experiments of MB with α-Fe_2O_3 obtained from PS-co-4-PVP and chitosan macromolecular precursors are summarized in Table 9. The highest extent of degradation of MB (98.6 %) at 150 min of irradiation time was achieved for α-Fe_2O_3 obtained from the PS-co-4-PVP$(FeCl_2)$y precursor in a 1:1 ratio.

Table 9. Kinetic data for the degradation of MB with α-Fe_2O_3 obtained from PS-co-4-PVP (1:1) and chitosan (1:1) macromolecular precursors (Adapted from reference [47]).

Photocatalyst	Apparent Photodegradation Rate Constant k (10^{-2} min^{-1})	Discoloration Rate η(%) at 60 min	Discoloration Rate η(%) at 150 min
α-Fe_2O_3 (PS-co-4-PVP)	1.2 ± 0.04	62.6	86.9
α-Fe_2O_3 (Chitosan)	2.1 ± 0.1	73.4	94.6

The size and morphology of the two systems were determined by electron microscopy studies, showing fused nanoparticles and 3D networks with average sizes of 150–200 nm for α-Fe_2O_3 from the precursor Chitosan($FeCl_2$) 1:1 and 55–100 nm for α-Fe_2O_3 from the precursor PS-co-4-PVP($FeCl_2$) 1:1. These morphologies show a random network of the surface area, quasi-linear nanoparticle chains that fold into larger porous powder particles [47]. It appears to be that for these Fe systems, the multifactorial relationship that holds this behavior could be the following:

$$PE = a \text{ bandgap} + b \text{ particle morphology} + c \text{ particle size} + d \text{ (Fe precursor)} \quad (3)$$

where the (Fe precursor) factor refers to the $FeCl_2$ or $FeCl_3$ metal salt source linked to the polymer. Once again, the most important factor dictating the photocatalyst efficiency of α-Fe_2O_3 toward the degradation of methylene blue is the *b* factor, more specifically, the material porosity. Table 9 shows that the bandgaps of α-Fe_2O_3 are similar; however, factor *a* could be less important. On the other hand, factors *c* and *d* could be somewhat significant.

3.3. NiO

NiO is a p-type semiconductor with E_g = 3.5 eV with multiple practical applications [57–60]. However, its bandgap can be modified by doping with other metal oxide semiconductors or by formation of nanocomposites in which one of the components would be in less quantity (mainly its photocatalyst properties) [59,60]. NiO has been used in catalysis, battery cathodes, fuel-cell electrodes, electrochromic films, electrochemical supercapacitors, and magnetic materials [59,60]. As these applications depend on its bandgap value and, in turn, the bandgap properties of superconductors depend on the environment of the metal oxide materials [61,62], there are no systematic, detailed studies on the effect of the medium on the bandgap. Although some $M_xO_y/M'_xO'_y$ have been prepared—where M_xO_y is a nanostructured metal oxide and $M'_xO'_y$ is a metal oxide matrix—no systematic effect of the matrix on the photocatalytic efficiency toward the degradation of organic dyes has been reported. By preparing the NiO/SiO_2, NiO/TiO_2, NiO/Al_2O_3, and NiO/glasses nanocomposites through a solid-state method, we have investigated the effect of the SiO_2, TiO_2, Al_2O_3, and $Na_{4.2}Ca_{2.8}(Si_6O_{18})$(glass) matrices on the photocatalytic properties of NiO toward the degradation of methylene blue [57]. The composites were prepared by solid-state thermal treatment of the Chitosan($NiCL_2$)$_x$/$M'_xO'$and PS-co-4-PVP($NiCL_2$)$_x$//$M'_xO'_y$ precursors, where $M'_xO'_y$ could be SiO_2, TiO_2, and Al_2O_3 glasses. Kinetic data for the photodegradation process of MB with NiO and with the NiO/SiO_2, NiO/TiO_2, NiO/Al_2O_3, and NiO/glasses composites are displayed in Table 10.

Table 10. Kinetic data for the photodegradation process of MB with NiO and with the NiO/SiO_2, NiO/TiO_2, NiO/Al_2O_3, and NiO/glasses composites (Adapted from reference [57]).

Photocatalyst	Apparent Photodegradation Rate Constant k (10^{-2} M·min^{-1})	Discoloration Rate (%)	R^2 Linear Fit (%)
NiO-chitosan [a]	2.4	71%	0.998
NiO-PS-4-PVP	2.2	68%	0.991
NiO/SiO_2-chitosan	2.3	69%	0.999
NiO/SiO_2-PS-4-PVP	1.6	48%	0.996
NiO/TiO_2-chitosan	2.9	91%	0.992
NiO/TiO_2-PS-4-PVP	2.6	81%	0.980
NiO/Al_2O_3-chitosan	1.5	45%	0.990
NiO/$Na_{4.2}Ca_{2.8}(Si_6O_{18})$	2.6	75%	0.990

[a] Nomenclature: Composite, hyphen (-), name of the precursor polymer.

As can be observed in Table 6, the NiO from the precursor containing the chitosan as a solid-state template produces much higher activity than the NiO sample arising from the PSP-4-PVP(NiO)$_x$ precursor. The polymer precursor clearly influences the photocatalytic activity. In this sense, using chitosan as a solid-state template produces much higher activity than the NiO sample arising from the PSP-4-PVP(NiO)$_x$ precursor. On the other hand, the most efficient photocatalytic activity was observed for the NiO/TiO_2 composite, with 90% degradation of methylene blue in 5 h.

In general, the photocatalytic activity shown in Table 10 is probably related to a matrix effect of NiO inside the different SiO_2, TiO_2, and Al_2O_3 matrices. Different matrices can influence NiO in different ways. For example, when the matrix is TiO_2, a p-n junction p-NiO/TiO_2 can be formed; this reduces the recombination rate of the photogenerated electron-hole pairs, which is known to enhance the photocatalytic activity of TiO_2 (see Figure 4) [60]. In the case of the NiO/TiO_2 composite, which has the highest catalytic behavior, the matrix effect may arise from the enhanced activity of TiO_2 by NiO. Therefore, in this case, NiO acts as a matrix in the active semiconductor for the degradation of methylene blue. On the other hand, the NiO/Al_2O_3 compound is one of the least efficient photocatalysts for the degradation of methylene blue, which is probably due to an insulating effect caused by Al_2O_3 that cuts off the communication between p-NiO and methylene blue to start the degradation of the dye. This is also in agreement with the low photocatalyst efficiency of the insulating SiO_2 matrix. An explanation for the results of the photocatalytic activity of the NiO/$Na_{4.2}Ca_{2.8}(Si_6O_{18})$ composite obtained from the Chitosan($NiCl_2·6H_2O)_x$//$Na_2O·CaO·SiO_2$ precursor is that $Na_{4.2}Ca_{2.8}(Si_6O_{18})$ has similar characteristics to those of SiO_2 as a matrix.

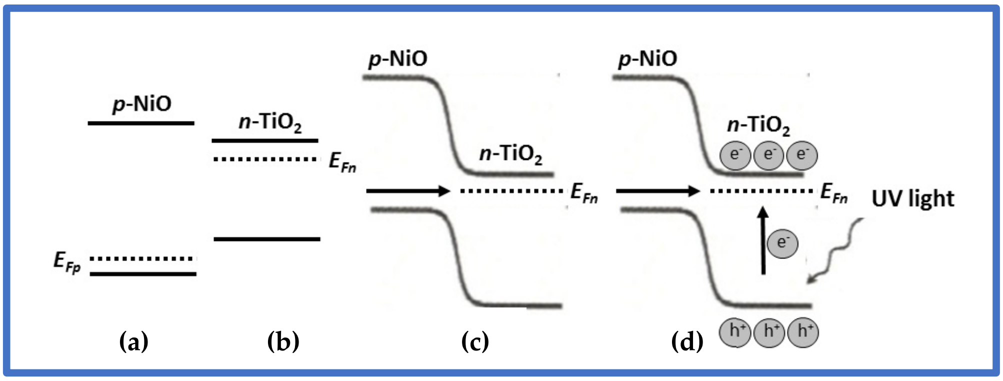

Figure 4. Schematic diagrams for (**a**) energy bands of p-NiO and (**b**) TiO_2 before contact, (**c**) formation of p-n junction and its energy diagram at equilibrium, and (**d**) transfer of holes from n-TiO_2 to p-NiO under UV irradiation (Adapted from reference [57]).

3.4. Precious Metal Oxides Ir, Rh, Re: IrO_2, Rh/RhO_2, Rh_2O_3, ReO_3

Among the metals in the periodic table, the so called precious—such as Ir, Rh, and Re, among others—are some of the most catalytically active [63]. Their activity is hugely enhanced at the nano-level [64,65]. These metals, as well as their metal oxides, exhibit high catalytic activity [63,65].

3.5. Ir

IrO_2 is a promising conducting oxide used, for example, as an electrode material in ferroelectric capacitors for nonvolatile memory applications [66]. However, to the best of our knowledge, there are no reports on its photocatalytic activity. The only related studies are those about the catalytic reduction of 4-Nitrophenol [67] and its electrochemical catalytic activity toward oxygen evolution [68]. As with the previous metal oxides, the iridium oxide for the catalytic experiments was prepared by thermal treatment of the Chitosan($IrCl_3)_x$ and PSP-4-PVP($IrCl_3)_x$ macromolecular precursors [55]. The as-prepared IrO_2has an adequate bandgap for the degradation of methylene blue under UV-visible irradiation (see Table 11). As previously mentioned, we have used this dye as a model dye to assay the photocatalytic properties of IrO_2. Kinetic data for the photodegradation process of MB with IrO_2 are displayed in Table 11. IrO_2 from the PVP precursor exhibits better photocatalytic activity (57% photodegradation in 300 min) than the IrO_2 from the chitosan precursor (38% photodegradation in 300 min). This effect was associated with the more porous morphology of IrO_2 from the PVP precursor [55].

Table 11. Kinetic data for the photodegradation process of MB with IrO_2, Rh/RhO_2, Rh/Rh_2O_3, and ReO_3.

Photocatalyst	Photodegradation Rate Constant k (10^{-3} M·min^{-1})	Discoloration Rate (%)	R^2 Linear Fit (%)	Ref.
IrO_2-PS-4-PVP	1.7	53%	0.995	[55]
IrO_2-chitosan	2.4	38%	0.991	[55]
Rh/RhO_2	[a]	78%	[b]	[56]
Rh_2O_3	[a]	70%	[b]	[56]
ReO_3-PS-4-PVP	2.8	64%	0.977	[54]
ReO_3-chitosan	2.8	53%	0.997	[54]

[a] Photodegradation rate constant k not informed. [b] Linear fit not informed.

3.6. Rh

In this case, the Rhodium oxides Rh/RhO_2 and Rh/Rh_2O_3 were obtained by pyrolysis of the PSP-4-PVP$(RhCl_3)_x$ and Chitosan$(RhCl_3)_x$ macromolecular precursors, respectively [56]. The bandgap values (see Table 12) are adequate for photocatalytic activity under UV-visible irradiation. The results (see Table 11) indicate that the Rh/RhO_2 sample exhibits better photocatalytic activity (78% photodegradation in 300 min) than the Rh/Rh_2O_3 one (70% photodegradation in 300 min). As the porosity of both materials is similar, the higher photocatalytic activity of Rh/RhO_2 could be due to its small particle size in the range 10–20 nm [56].

Table 12. Bandgap for the Ir, Rh, and Re oxides.

Photocatalyst	Bandgap (eV)	Ref.
ReO_3	4.36	[54]
IrO_2	2.4–2.6	[55]
Rh/RhO_2	3.7	[56]
Rh_2O_3	3.0	[56]

3.7. Re

ReO_3 for the photocatalytic essays was obtained by solid-state thermal treatment of the Chitosan$(ReCl_3)_x$ and PSP-4-PVP$(ReCl_3)_x$ macromolecular precursors [54]. The bandgap for ReO_3 indicates an adequate value for UV-visible photoactivation (see Table 12). ReO_3 was also found to catalyze the photodegradation of MB with an efficiency of 53% and 64% in 300 min for the chitosan and PVP precursors, respectively (see Table 11). ReO_3 is an unusual transition metal oxide as it presents a metallic behavior with conductivity close to that of copper [69]. Therefore, nanoparticles of rhenium trioxide produce a SERS (surface-enhanced Raman spectra) effect on some organic compounds, such as pyridine [70]. Despite this, their catalytic activity has only been proved in the catalytic degradation of methyl orange [71].

3.8. Th

Among the actinides oxides, thoria is an important and promising material used in ceramic catalyst sensor solid electrolytes, catalysis, optical materials, and the traditional nuclear industry [72–75]. The thorium oxide was prepared by thermal treatment of the Chitosan $Th(NO_3)_4$ and PS-co-4-PVP$Th(NO_3)_4$ macromolecular precursors at 800 °C. The ThO_2/SiO_2 and ThO_2/TiO_2 composites were also synthesized by pyrolysis of the Chitosan $Th(NO_3)_4//MO_2$ andPS-co-4-PVP $Th(NO_3)_4//MO_2$ macromolecular composites, where MO_2 is SiO_2 or TiO_2.

To the best of our knowledge, no photocatalytic studies on ThO_2, ThO_2/SiO_2, or ThO_2/TiO_2 have been reported. Regarding thoria, scarce literature data have been reported. As for ThO_2 nanoparticles, Aller et al. [76] report values ranging from 5.13 eV to 4.5 eV, while for ThO_2 thin films, Buono-Core et al. [77] report values from 4.5 eV to 4.61 eV. However, some of these values are theoretical calculations. Using the solid-state UV-visible absorption and the Tauc plot for ThO_2, a value of 5.66 eV is estimated for the chitosan polymer precursor and 5.76 eV for the PS-4-co-PVP polymer precursor.

With this in mind, using UV-visible radiation, some catalytic activity for ThO_2 could be expected. In fact, the values for the catalytic results are shown in Table 13. The values for the ThO_2/SiO_2 and ThO_2/TiO_2 nanocomposites are also shown for comparison. On the other hand, the bandgap values for thoria included in TiO_2 as matrix exhibited values of 3.14 eV and 3.15 eV for the ThO_2/TiO_2 composites from chitosan and PS-4-co-PVP polymer precursors, respectively. These values are lower than those of ThO_2 and ThO_2/SiO_2; however, as Buono-Core et al. point out [77], the optical bandgap energy is very sensitive to the preparation method and the experimental parameters applied in the synthesis [77]. In fact, Mahmoud reported a value of 3.82 eV for ThO_2 prepared by a spray pyrolysis technique [78]. The estimated rate constant for the degradation of methylene blue in the presence of thorium prepared without the SiO_2 and TiO_2 matrices is greater than that of the pristine compounds, suggesting that the structural modification and synergy of the inorganic components play a fundamental role. This is related to the increase in the photocatalytic efficiency of the semiconductor as a result of the greater number of active sites provided by the (ThO_2) PS-4-co-PVP and (ThO_2) chitosan precursors.

Table 13. Kinetic data for the photodegradation process of MB with ThO_2 and with the ThO_2/SiO_2, ThO_2/TiO_2 composites (Adapted from reference [21]).

Photocatalyst	E_g (eV)	Apparent Photodegradation	Discoloration Rate (%)	R^2 Linear Fit (%)
ThO_2(chitosan precursor)	5.66	3.7×10^{-3}	67	0.992
ThO_2 (PS-4-PVP precursor)	5.75	2.2×10^{-3}	66	0.967
ThO_2/SiO_2 (chitosan precursor)	5.50	7.7×10^{-4}	24	0.979
ThO_2/SiO_2 (PS-4-PVP precursor)	5.6	8.5×10^{-4}	25	0.923
ThO_2/TiO_2 (chitosan precursor)	3.14	1.4×10^{-3}	39	0.815
ThO_2/TiO_2 (PS-4-PVP precursor)	3.14	8.7×10^{-4}	27	0.941

In general and according to the examples shown here, the efficiency in photocatalysis using photocatalyst semiconductor oxides obtained by a solid method is higher than that exhibited by the same photocatalysts obtained by solution methods. This may be due to the high porosity of the catalysts obtained by the solid state method.

3.9. Heterojunction Structure

These structures are formed by coupling two semiconductors whose band structures are aligned in such a way that they allow for an enhanced charge separation compared to the single system. A maximum of two alignments are feasible with this binary combination, viz., type I and type II [79–82]. Figure 5 shows a schematic of the band alignment of the nanocomposites for both heterostructures. In the type I alignment, both the VB and CB edge potential of either semiconductor lies within the bandgap of the other semiconductor, as the latter possesses a wider bandgap. Since one has lower VB and CB potentials than the other, both bands act as hole and electron collecting sites, as is shown in Figure 5. In the type II heterostructure, the CB position of the first semiconductor lies above that of the second, whereas its VB lies within the bandgap of the second. Therefore, the photogenerated holes tend to migrate to the VB of the first one, whereas the excited electrons tend to migrate to the CB of the second. The mentioned band position and migration of the charge carriers are depicted in Figure 5b. In general, the type II heterostructure is widely preferred because it allows the migration of electrons and holes in the opposite direction (see Figure 5b) [79–82].

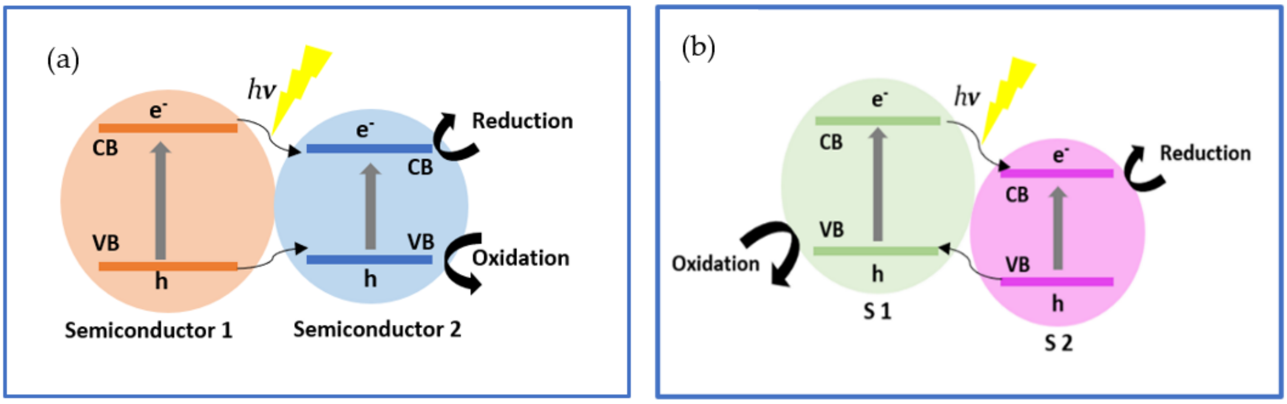

Figure 5. Schematic illustration of the type-I (**a**) and Type II (**b**) band alignments.

Some examples of both type I and type II band alignments are presented and discussed in reference [81].

3.10. Photocatalyst Mechanism of Dye Degradation by Nanostructures

In general, the system of heterogeneous photocatalysis using semiconductor materials consists of a light-harvesting antenna and several active species to facilitate pollutant degradation [83]. The series of chain oxidative-reductive reactions that occur at the photon-activated surface has been broadly proposed as:

$\text{Photocatalyst} + h\nu \rightarrow h^+ + e^-$
$h^+ + H_2O \rightarrow {}^*OH + H^+$
$h^+ + OH^- \rightarrow {}^*OH$
$h^+ + \text{Pollutant} \rightarrow (\text{Pollutant})^+$
$e^- + O_2 \rightarrow {}^*O_2{}^-$
${}^*O_2{}^- + H^+ \rightarrow {}^*OOH^-$
$2\ {}^*OOH \rightarrow O_2 + H_2O_2$
$H_2O_2 + {}^*O_2{}^- \rightarrow {}^*OH + OH^- + O_2$
$H_2O_2 + h\nu \rightarrow 2\ {}^*OH$

Hence, the final reaction is:

$$\text{Pollutant} + ({}^\bullet OH, h^+, {}^\bullet OOH \text{ or } O_2{}^-) \rightarrow \text{degradation products}$$

which produces the degradation of the pollutant.

When the semiconductor is irradiated by an input light possessing ultra-band-gap energy ($h\nu > E_g$), a valence band (VB) electron (e^-) is excited to the conduction band (CB), leaving behind a photogenerated hole (h^+) at the VB. Accordingly, the produced e^-/h^+ pairs are able to migrate to the surface of the semiconductor and participate in redox reactions.

The photocatalytic reaction usually involves three main active species: a hydroxyl radical (${}^\bullet OH$), h^+, and a superoxide radical (${}^\bullet O_2{}^-$), where ${}^\bullet OH$ is the primary oxidant in the photocatalytic degradation of the pollutant in the aqueous solution. ${}^\bullet OH$ radicals are normally generated via two routes: (i) H_2O and OH^- in a water environment are readily oxidized by photogenerated h^+ to form ${}^\bullet OH$ radicals; (ii) O_2 present in an aqueous solution is reduced by photogenerated e^- to form O_2 radicals, which subsequently react with h^+ forming ${}^\bullet OOH$ radicals, whose further decomposition produces ${}^\bullet OH$ radicals.

Complementary to what was discussed above, two interesting reviews [84,85] analyze the photocatalytic properties of the TiO_2 system incorporated in a carbon gel matrix and covalent organic frameworks (COFs). In Dongge et al., although still in its incipient stage in comparison with other traditional inorganic metal oxides, titania is proposed as having some advantages such as having a high surface due to the high porosity of the carbon gel matrix. In the second case, Yuhang et al. point out that even when COFs are highly porous and crystalline polymeric materials, they are photocatalytic systems different from nanostructured metal oxide semiconductors, and are a valid alternative in environmental remediation. Meanwhile, recent investigations [86,87] have proven that photocatalysis of nanostructured metal oxides is being increasingly adopted.

4. Conclusions

Nanostructured metal oxides play an important role in the environmental decontamination of organic dyes. An alternative route that often improves photocatalytic efficiency is the use of photocatalysts based on metal oxides obtained by a solid-state method. Specifically, the solid-state method based on the thermal treatment of Chitosan·MXn and PS-co-4-PVP MXn precursors affords pure nanostructured metal oxides M_xO_y, which are often more efficient photocatalysts than the respective M_xO_y obtained by other solution methods. It was found that the photocatalytic efficiency depends on the nature of the MXn precursor salts and the calcination temperature, as in the case of TiO_2, where the most efficient photocatalyst was the one obtained from the Chitosan $TiSO_4$ precursor pyrolyzed at 800 °C. The efficiency of most of the studied photocatalysts can be described by the following relationship:

$$PE = a \text{ band gap} + b \text{ particle morphology} + c \text{ particle size} + d \text{ crystalline phase} + e \text{ pyrolysis temperature} \quad (4)$$

where *PE* is the photocatalyst efficiency. In particular, for a nanostructured metal oxide semiconductor photocatalyst obtained using our solid-state method, morphology is more important than the bandgap. In turn, when using the solid-state preparation method of the metal oxide photocatalyst, the temperature often modulates the morphology. This can, for example, generate a highly porous morphology, thus causing a very efficient photocatalytic activity.

However, research on this topic is a challenge since the parameters that induce a more efficient photocatalysis in solid-state synthesis are not fully known. An achievement in this matter could be a significant advance for environmental decontamination.

Author Contributions: C.D., M.L.V. and M.S. conceptualized, wrote, and agreed to the published version of the manuscript. All authors have read and agreed to the published version of the manuscript.

Funding: University of Chile Department of Chemistry, Faculty of Sciences.

Data Availability Statement: This study did not report any data.

Conflicts of Interest: The authors declare no conflict of interest.

References

1. Hornyak, G.; Tibbals, H.F.; Dutta, J.; Moore, J. *Introduction to Nanoscience and Nanotechnology*; CRC Press: Boca Raton, FL, USA, 2008.
2. Altavilla, C.; Ciliberto, E. *Inorganic Nanoparticles*; CRC Press: Boca Raton, FL, USA, 2011.
3. Khin, M.A.; Sreekumaran Nair, A.; Jagadeesh Babu, V.; Murugan, R.; Ramakrishna, S. A review on nanomaterials for environmental remediation. *Energy Environ. Sci.* **2012**, *5*, 8075. [CrossRef]
4. Edelstein, A.S.; Cammarata, R.C. *Nanomaterials, Synthesis and Applications*; Institute of Physics Publishing Bristol: Arrowsmith, UK, 2002.
5. Cao, G. *Nanostructures and Nanomaterial, Synthesis, Properties and Applications*; Imperial College Press: London, UK, 2004.
6. Ahmada, R.; Ahmadb, Z.; Ullah Khanb, A.; Riaz Mastoi, N.; Aslama, M.; Kim, J. Photocatalytic systems as an advanced environmental remediation: Recent developments, limitations and new avenues for applications. *J. Environ. Chem. Eng.* **2016**, *4*, 4143–4164. [CrossRef]
7. Adeyemo, A.A.; Adeoye, I.O.; Bello, O.S. Metal organic frameworks as adsorbents for dye adsorption, overview, prospects and future challenges. *Toxicol. Environ. Chem.* **2012**, *94*, 1846–1863. [CrossRef]
8. Chong, M.N.; Jin, B.; Chow, C.W.; Saint, C. Recent developments in photocatalytic water treatment technology: A review. *Water Res.* **2010**, *44*, 2997–3027. [CrossRef] [PubMed]
9. Gunten, V. Oxidation Processes in Water Treatment: Are We on Track? *Environ. Sci. Technol.* **2018**, *52*, 5062–5075. [CrossRef]
10. Nikam, A.V.; Prasad, B.L.V.; Kulkarnia, A.A. Wet Chemical Synthesis of Metal Oxide Nanoparticles, A Review. *Cryst. Eng. Comm.* **2018**, *20*, 5091–5107. [CrossRef]
11. Oska, G. Metal oxide nanoparticles, synthesis, characterization and application. *J. Sol. Gel. Sci. Techn.* **2006**, *37*, 161–164. [CrossRef]

12. Diaz, C.; Valenzuela, M.L.; Laguna-Bercero, M.A. Solid-State Preparation of Metal and Metal Oxides Nanostructures and Their Application in Environmental Remediation. *Int. J. Mol. Sci.* **2022**, *23*, 1093. [CrossRef]
13. Wang, C.; Li, J.; Liang, X.; Zhang, Y.; Guo, G. Photocatalytic Organic Pollutants Degradation in Metal–Organic Frameworks. *Energy Environ. Sci.* **2014**, *7*, 2831–2867. [CrossRef]
14. Liu, X.; Iocozzia, J.; Wang, Y.; Cui, X.; Chen, Y.; Zhao, S.; Li, Z.; Lin, Z. Noble metal–metal oxide nanohybrids with tailored nanostructures for efficient solar energy conversion, photocatalysis and environmental remediation. *Energy Environ. Sci.* **2017**, *10*, 402–434. [CrossRef]
15. Gaya, U.I.; Abdullah, A.H. Heterogeneous photocatalytic degradation of organic contaminants over titanium dioxide: A review of fundamentals, progress and problems. *J. Photochem. Photobiol. C* **2008**, *9*, 1–12. [CrossRef]
16. Khan, M.M.; Adil, S.F.; Al-Mayouf, A. Metal oxides as photocatalysts. *J. Saudi Chem. Soc.* **2015**, *19*, 462–464. [CrossRef]
17. Preeti, S.; Abdullah, M.M.; Saiga, I. Role of Nanomaterials and Their Applications as Photo-catalst and Sensor, A review. *Nano Res. Appl.* **2016**, *2*, 1–10.
18. Lany, S. Semiconducting transition metal oxides. *J. Phys. Condens. Matter* **2015**, *27*, 283203. [CrossRef] [PubMed]
19. Wang, J.; Wang, Y.; Huang, Y.; Peijnenburg, J.G.; Chen, J.; Li, X. Development of a nano-QSPR model to predict band gaps of spherical metal oxide nanoparticles. *RSC Adv.* **2019**, *9*, 8426–8434. [CrossRef]
20. Tran, F.; Blaha, P. Accurate Band Gaps of Semiconductors and Insulators with a Semilocal Exchange-Correlation Potential. *Phys. Rev. Lett.* **2009**, *102*, 226401. [CrossRef] [PubMed]
21. Díaz, C.; Valenzuela, M.L.; Laguna-Bercero, M.A.; Mendoza, K.; Cartes, P. Solventless preparation of thoria, their inclusion inside SiO_2 and TiO_2, their luminiscent properties and their photocataltytic behavior. *ACS Omega* **2021**, *6*, 9391–9400. [CrossRef]
22. Guo, Y.; Ma, L.; Mao, K.; Ju, M.; Bai, Y.; Zhao, J.; Zeng, X. Eighteen functional monolayer metal oxides: Wide bandgap semiconductors with superior oxidation resistance and ultrahigh carrier mobility. *Nanoscale Horiz.* **2019**, *4*, 592–600. [CrossRef]
23. Allende, P.; Laguna, M.A.; Barrientos, L.; Valenzuela, M.L.; Díaz, C. Solid state tuning Morphology, Crystal Phase and Size through Metal Macromolecular Complexes and Its Significance in the Photocatalytic Response. *ACS Appl. Energy Mater.* **2018**, *1*, 3159–3170. [CrossRef]
24. Ikram, M.; Rashid, M.; Haider, A.; Naz, S.; Haider, J.; Raza, A.; Ansard, M.T.; Uddin, K.; Nageh, M.; Ali, M.; et al. A review of photocatalytic characterization, and environmental cleaning, of metal oxide nanostructured materials. *Sustain. Mater. Technol.* **2021**, *30*, e00343. [CrossRef]
25. Ferreira, D.L.; Sousa, J.C.L.; Maronesi, R.N.; Bettini, J.; Schiavon, M.A.; Silva, A.G. Size-dependent bandgap and particle size distribution of colloidal semiconductor nanocrystals. *J. Chem. Phys.* **2017**, *147*, 154102–154111. [CrossRef] [PubMed]
26. Ahmad, M.; Zhu, J. ZnO based advanced functional nanostructures: Synthesis, properties and applications. *J. Mater. Chem.* **2011**, *21*, 599–614. [CrossRef]
27. Wang, Z.L. Zinc oxide nanostructures: Growth, properties and applications. *J. Phys. Condens. Matter* **2004**, *16*, R829–R858. [CrossRef]
28. Chen, X.; Mao, S.S. Titanium Dioxide Nanomaterials, Synthesis, Properties, Modifications, and Applications. *Chem Rev.* **2007**, *107*, 2891–2959. [CrossRef] [PubMed]
29. Ismail, A.A.; Bahnemannb, D.W. Mesoporous titania photocatalysts, preparation, characterization and reaction mechanisms. *J. Mater. Chem.* **2011**, *21*, 11686–11707. [CrossRef]
30. He, H.; Liu, C.; Dubois, K.; Jin, T.; Louis, M.E.; Li, G. Enhanced Charge Separation in Nanostructured TiO_2 Materials for Photocatalytic and Photovoltaic Applications. *Ind. Eng. Chem. Res.* **2012**, *51*, 11841–11849. [CrossRef]
31. Ge, M.; Cao, C.; Huang, J.; Li, S.; Chen, Z.; Zhang, K.; Al-Deyab, S.S.; Lai, Y. A Review of One-dimensional TiO_2 Nanostructured Materials for Environmental and Energy Applications. *J. Mater. Chem. A* **2016**, *4*, 6772–6801. [CrossRef]
32. Díaz, C.; Valenzuela, M.L. *Metallic Nanostructures Using Oligo and Polyphosphazenes as Template or Stabilizer in Solid State in Encyclopedia of Nanoscience and Nanotechnology*; Nalwa, H.S., Ed.; American Scientific Publishers: Valencia, CA, USA, 2010; Volume 16, pp. 239–256.
33. Díaz, C.; Valenzuela, M.L. Macromolecular Complexes MXn Polymer as solid state precursors of metal and metal oxides nanostructures. In *Book of CRC Concise Encyclopedia of Nanotechnology*; Kharisov, B.I., Kharisov, O.V., Mendez, U., Eds.; CRC Press: Boca Raton, FL, USA, 2016; Chapter 42; pp. 504–524.
34. Ray, C.; Pai, T. Recent advances of metal–metal oxide nanocomposites and their tailored nanostructures in numerous catalytic applications. *J. Mater. Chem.* **2017**, *5*, 9465–9478. [CrossRef]
35. Díaz, C.; Valenzuela, M.L. Small-Molecule and High-Polymeric Phosphazenes containing oxypyridine side groups and their organometallic derivatives; Useful precursors for metal nanostructured materials. *Macromolecules* **2006**, *39*, 103–111. [CrossRef]
36. Díaz, C.; Valenzuela, M.L. Organometallic Derivatives of Polyphosphazenes as Precursors for Metallic Nanostructured Materials. *J. Inorg. Organomet. Polym. Mater.* **2006**, *16*, 419–435. [CrossRef]
37. Díaz, C.; Valenzuela, M.L.; Zuñiga, L.; O'Dwyer, C. Organometallic derivatives of cyclotriphosphazene as precursors of Nanostructured metallic materials: A new solid state Method. *J. Inorg. Organomet. Polym. Mater.* **2009**, *19*, 507–520. [CrossRef]
38. Díaz, C.; Valenzuela, M.L.; Lavayen, V.; O'Dwyer, C. Layered Graphitic Carbon Host Formation during Liquid-free Solid State Growth of Metal Pyrophosphates. *Inorganic Chem.* **2012**, *51*, 6228–6236. [CrossRef] [PubMed]
39. Díaz, C.; Valenzuela, M.L.; Cáceres, S.; O´Dwyer, C. Solution and surfactant-free growth of supported high index facet SERS active nanoparticles of rhenium by phase demixing. *J. Mater. Chem. A* **2013**, *1*, 1566–1572.

40. Díaz, C.; Valenzuela, M.L.; Cáceres, S.; O´Dwyer, C.; Diaz, R. Solvent and stabilizer free growth of Ag and Pd nanoparticles using Metallic salts/cyclotriphosphazenes mixtures. *Mater. Chem. Phys.* **2013**, *143*, 124–132. [CrossRef]
41. Díaz, C.; Valenzuela, M.L.; Zuñiga, L.; O'Dwyer, C. Solid State Pathways to Complex Shape Evolution and Tunable Porosity During Metallic Crystal Growth. *Sci. Rep.* **2013**, *2642*, 1–8.
42. Díaz, C.; Valenzuela, M.L. Nanostructures: Properties: Production Methods and Application. In *Organometallic-Metallic-Cyclotriphosphazene Mixtures: Solid-State Method for Metallic Nanoparticle Growth*; Nova Science Publishers: New York, NY, USA, 2013; Chapter 5.
43. Díaz, C.; Valenzuela, M.L. *A General Solid-State Approach to Metallic, Metal Oxides and Phosphates Nanoparticles in Advances in Chemical Research*; Nova Science Publishers: New York, NY, USA, 2011.
44. Díaz, C.; Valenzuela, M.L. A general Solid-State approach to Metallic, Metal oxides and Phosphate nanoparticles Gold Nanoparticles: Properties Synthesis and Fabrication. In *Solution and Solid State Methods to Prepare Au Nanoparticles: A comparison Chow PE*; Nova Science Publishers: New York, NY, USA, 2010; Chapter 14.
45. Díaz, C.; Valenzuela, M.L.; Lavayen, V.; Mendoza, K.; Peña, O.; O'Dwyer, C. Nanostructured copper oxides and phosphates from a new solid-state route. *Inorg. Chim. Acta* **2011**, *377*, 5–11. [CrossRef]
46. Díaz, C.; Platoni, S.; Molina, A.; Valenzuela, M.L.; Geaney, H.; O'Dwyer, C. Novel Solid-State Route to Nanostructured Tin, Zinc and Cerium Oxides as Potential Materials for Sensors. *J. Nanosci. Nanotechnol* **2014**, *14*, 7648–7675. [CrossRef]
47. Díaz, C.; Barrera, G.; Segovia, M.; Valenzuela, M.L.; Osiak, M.; O'Dwyer, C. Solvent-less method for efficient photocatalytic α-Fe_2O_3 nanoparticles for using macromolecular polymeric precursors. *New J. Chem.* **2016**, *40*, 6768–6776. [CrossRef]
48. Díaz, C.; Valenzuela, M.L.; Laguna, M.A.; Orera, A.; Bobadilla, D.; Abarca, S.; Peña, O. Synthesis and Magnetic Properties of Nanostructured metallic Co, Mn and Ni oxide materials obtained from solid-state macromolecular complex precursors. *RSC Adv.* **2017**, *7*, 27729–27736. [CrossRef]
49. Díaz, C.; Valenzuela, M.L.; Bobadilla, D.; Laguna-Bercero, M.A. Bimetallic Au//Ag Alloys Inside SiO_2 using a solid-state method. *J. Clust. Chem.* **2017**, *28*, 2809–2815. [CrossRef]
50. Díaz, C.; Valenzuela, M.L.; Garcia, C.; De la Campa, R.; Soto, A.-P. Solid-state synthesis of pure and doped lanthanides oxide nanomaterials by using polymer templates. Study of their luminescent properties. *Mater. Lett.* **2017**, *209*, 111–114. [CrossRef]
51. Díaz, C.; Valenzuela, M.L.; Segovia, M.; De la Campa, R.; Soto, A.-P. Solution, Solid-State Two Step Synthesis and Optical Properties of ZnO and SnO Nanoparticles and Their Nanocomposites with SiO_2. *J. Clust. Sci.* **2018**, *29*, 251–266. [CrossRef]
52. Díaz, C.; Carrillo, D.; De la Campa, R.; Soto, A.-P.; Valenzuela, M.L. Solid-State synthesis of $LnOCl/Ln_2O_3$ (Ln = Eu, Nd) by using chitosan and PS-co-P4VP as polymeric supports. *J. Rare Earth* **2018**, *36*, 1326–1332. [CrossRef]
53. Allende, P.; Barrientos, L.; Orera, A.; Laguna-Bercero, M.A.; Salazar, N.; Valenzuela, M.L.; Diaz, C. TiO_2/SiO_2 Composite for Efficient Protection of UVA and UVB Rays Through of a Solvent-Less Synthesis. *J. Clust. Sci.* **2019**, *30*, 1511–1517. [CrossRef]
54. Díaz, C.; Valenzuela, M.L.; Cifuentes-Vaca, O.; Segovia, M.; Laguna-Bercero, M.A. Incorporation of Nanostructured ReO_3 in Silica Matrix and Their Activity Toward Photodegradation of Blue Methylene. *J. Inorg. Organomet. Polym. Mater.* **2020**, *30*, 1726–1734. [CrossRef]
55. Diaz, C.; Valenzuela, M.L.; Cifuentes-Vaca, O.; Segovia, M.; Laguna-Bercero, M.A. Iridium nanostructured metal oxide, its inclusion in Silica matrix and their activity toward Photodegradation of Methylene Blue. *Mater. Chem. Phys.* **2020**, *252*, 123276–123286. [CrossRef]
56. Díaz, C.; Valenzuela, M.L.; Cifuentes-Vaca, O.; Segovia, M. Polymer precursors effect in the macromolecular metal-polymer on the $Rh/RhO_2/Rh_2O_3$ phase using solvent-less synthesis and its photocatalytic activity. *J. Inorg. Organomet. Polym. Mater.* **2020**, *30*, 4702–4708. [CrossRef]
57. Díaz, C.; Valenzuela, M.L.; Cifuentes-Vaca, O.; Segovia, M.; Laguna-Bercero, M.A. Incorporation of NiO into SiO_2, TiO_2, Al_2O_3, and $Na_{4.2}Ca_{2.8}(Si_6O_{18})$ Matrices, Medium Effect on the Optical Properties and Catalytic Degradation of Methylene Blue. *Nanomaterials* **2020**, *10*, 2470. [CrossRef]
58. Sietsma, J.R.A.; Meeldijk, J.D.; Den Breejen, J.P.; Versluijs-Helder, M.; Jos van Dillen, A.; De Jongh, P.E.; De Jong, K.P. The Preparation of Supported NiO and Co_3O_4 Nanoparticles by the Nitric Oxide Controlled Thermal Decomposition of Nitrates. *Ang. Chem Int. Ed.* **2007**, *46*, 4547–4549. [CrossRef]
59. Zhang, Z.; Shao, C.; Li, X.; Wang, C.; Zhang, M.; Liu, Y. Electrospun Nanofibers of p~Type NiO/n~Type ZnO Heterojunctions with Enhanced Photocatalytyc Activity. *ACS. Appl. Mater. Interface Sci.* **2010**, *10*, 2915–2923. [CrossRef]
60. Yu, J.; Wang, W.; Cheng, B. Synthesis and Enhanced Photocatalytic Activity of a Hierarchical Porous Flowerlike p–n Junction NiO/TiO_2 Photocatalyst. *Chem. Asian* **2010**, *5*, 2499–2506. [CrossRef] [PubMed]
61. Bonomo, M.; Dini, D.; Decker, F. Electrochemical and Photoelectrochemical Properties of Nickel Oxide (NiO) With Nanostructured Morphology for Photoconversion Applications. *Front. Chem.* **2018**, *6*, 601. [CrossRef] [PubMed]
62. Kelly, K.L.; Coronado, E.; Zhao, L.L.; Schatz, G. The optical properties of metal nanoparticles: The influence of size, shape, and dielectric environment. *J. Phys. Chem.* **2003**, *107*, 668–677. [CrossRef]
63. Cotton, F.A.; Wilkinson, G. *Advanced Inorganic Chemistry*; John Wiley and Sons: New York, NY, USA, 1980; Chapters 22 and 30.
64. Jin, R. The impacts of nanotechnology on catalysis by precious metal nanoparticles. *Nanotechnol. Rev.* **2012**, 31–56. [CrossRef]
65. Fernandez-Garcia, M.; Martinez-Arias, A.; Hanson, J.; Rodriguez, C. Nanostructured Oxides in Chemistry: Characterization and Properties. *Chem. Rev.* **2004**, *104*, 4063–4104. [CrossRef]

66. Chen, R.S.; Korotcov, A.; Huiang, Y.S.; Tsai, D. One-dimensional conductive IrO_2. *Nanocrystals Nanotechnol.* **2006**, *17*, 67–87. [CrossRef]
67. Xu, D.; Diao, P.; Jin, T.; Wu, Q.; Liu, X.; Guo, X.; Gong, H.; Li, F.; Xiang, M.; Ronghai, Y. Iridium oxide nanoparticles and Iridium/Iridium Oxide Nanocompósites: Photochemical Fabrication and Application in Catalytic Rediction of Notrophenol. *ACS Appl. Interfaces* **2015**, *7*, 16738–16749. [CrossRef]
68. Zhao, Y.; Hernandez, E.A.; Vargas-Barbosa, N.M.; Dysart, J.L.; Mallouk, T.E. A high yield Synthesis of ligand-free iridium oxide nanoparticles with high electrocatalytic activity. *J. Phys. Chem. Lett.* **2011**, *2*, 402–406. [CrossRef]
69. Biswas, K.; Rao, C.N. Metallic ReO_3 Nanoparticles. *J. Phys. Chem. B* **2006**, *110*, 842–845. [CrossRef]
70. Biswas, K.; Bhat, S.V.; Rao, C.N. Surface-Enhanced Raman Spectra of Aza-aromatics on Nanocrystals of Metallic ReO_3. *J. Phys. Chem. C* **2006**, *111*, 5689–5693. [CrossRef]
71. Biswas, K.; Rao, C.N. Synthesis and Characterization of Nanocrystals of the Oxide Metals, RuO_2, IrO_2, and ReO_3. *J. Nanosci. Nanotechniol* **2007**, *7*, 1969–1974. [CrossRef] [PubMed]
72. Lin, Z.-W.; Kuang, Q.; Lian, W.; Jiang, Z.-Y.; Xie, Z.-X.; Huang, R.-B.; Zheng, L.-S. Preparation and Optical Properties of ThO_2 and Eu-Doped ThO_2 Nanotubes by the Sol−Gel Method Combined with Porous Anodic Aluminum Oxide Template. *J. Phys. Chem. B* **2006**, *110*, 23007–23011. [CrossRef] [PubMed]
73. Hudry, D.; Apostolidis, C.; Walter, O.; Gouder, T.; Courtois, E.; Kubel, C.; Meyer, D. Non-aqueous Synthesis of Isotropic and Anisotropic Actinide Oxide Nanocrystals. *Chem. Eur. J.* **2012**, *18*, 8283–8287. [CrossRef] [PubMed]
74. Hudry, D.; Apostolidis, C.; Walter, O.; Gouder, H.; Courtois, E.; Kubel, C.; Meyer, D. Controlled Synthesis of Thorium and Uranium Oxide Nanocrystals. *Chem. Eur. J.* **2013**, *19*, 5297–5305. [CrossRef]
75. Tripathi, V.K.; Narajan, R. Sol–Gel Synthesis of High-Purity Actinide Oxide ThO_2 and Its Solid Solutions with Technologically Important Tin and Zinc Ions. *Inorg. Chem.* **2016**, *55*, 12798–12906. [CrossRef]
76. Pereira, F.J.; Castro, M.A.; Vazquez, M.D.; Deban, L.; Aller, A.J. Optical properties of ThO_2–based nanoparticles. *J. Lumin.* **2017**, *184*, 169–178. [CrossRef]
77. Huentupil, Y.; Cabello-Guzman, G.; Chornik, B.; Arancibia, R.; Buono-Cuore, G.E. Photochemical deposition, characterization and optical properties of thin films of ThO_2. *Polyhedron* **2019**, *157*, 225–231. [CrossRef]
78. Mahmoud, S.A. Characterization of thorium dioxide thin films prepared by the spray pyrolysis technique. *Solid State Sci.* **2002**, *4*, 221–228. [CrossRef]
79. Li, H.; Zhou, Y.; Tu, W.; Ye, J.; Zou, Z. State-of-the-art progress in diverse heterostructured photocatalysts toward promoting photocatalytic performance. *Adv. Funct. Mater.* **2014**, *25*, 998–1013. [CrossRef]
80. Wang, Y.; Wang, Q.; Zhan, X.; Wang, F.; Safdar, M.; He, J. Visible light driven type II heterostructures and their enhanced photocatalysis properties: A review. *Nanoscale* **2013**, *5*, 8326–8339. [CrossRef]
81. Rani, A.; Reddy, R.; Sharma, U.; Mukherjee, P.; Mishra, P.; Kuila, A.; Sim, L.C.; Saravanan, P. A review on the progress of nanostructure materials for energy harnessing and environmental remediation. *J. Nanostructure Chem.* **2018**, *8*, 255–291. [CrossRef]
82. Li, H.; Tu, W.; Zhou, Y.; Zou, Z. Z-Scheme Photocatalytic Systems for Promoting Photocatalytic Performance: Recent Progress and Future Challenge. *Adv. Sci.* **2016**, *3*, 1500389. [CrossRef] [PubMed]
83. Dong, S.; Feng, J.; Fan, M.; Pi, Y.; Hu, L.; Han, X.; Liu, M.; Sun, J.; Sun, J. Recent developments in heterogeneous photocatalytic water treatment using visible light responsive photocatalysts: A review. *RSC Adv.* **2015**, *5*, 14610–14630. [CrossRef]
84. Dongge, M.; Jundan, L.; Anan, L.; Chuncheng, C. Carbon Gels-Modified TiO2: Promising Materials for Photocatalysis Applications. *Materials* **2020**, *13*, 1734.
85. Yuhang, Q.; Dongge, M. Covalent Organic Frameworks: New Materials Platform for Photocatalytic Degradation of Aqueous Pollutants. *Materials* **2021**, *14*, 5600.
86. Nunes, D.; Pimentel, A.; Branquinho, R.; Fortunato, E.; Martins, R. Metal Oxide-Based Photocatalytic Paper: A Green Alternative for Environmental Remediation. *Catalysts* **2021**, *11*, 504. [CrossRef]
87. Shah, M.; Estrella, L.; Alemaida, I.; Lisin, A.; Moiseev, N.; Ahmadi, M.; Nazari, M.; Wali, M.; Zaheb, H.; Senjyu, T. Photocatalytic Applications of Metal Oxides for Sustainable Environmental Remediation. *Metals* **2021**, *11*, 80.